tvst

Retina

Evaluating Blood Flow Speed in Retinal Microaneurysms Secondary to Diabetic Retinopathy Using Variable Interscan Time Analysis OCTA

Hiroyuki Takahashi[1–3], Yunchan Hwang[2], Jungeun Won[2], Muhammad Usman Jamil[1], Antonio Yaghy[1], Michelle C. Liang[1], Caroline R. Baumal[1], Andre J. Witkin[1], Kyoko Ohno-Matsui[3], Jay S. Duker[1], James G. Fujimoto[2], and Nadia K. Waheed[1]

[1] New England Eye Center, Tufts Medical Center, Boston, MA, USA
[2] Department of Electrical Engineering and Computer Science, Research Laboratory of Electronics, Massachusetts Institute of Technology, Cambridge, MA, USA
[3] Department of Ophthalmology and Visual Science, Graduate School of Medical and Dental Sciences, Institute of Science Tokyo, Tokyo, Japan

Correspondence: Nadia K. Waheed, New England Eye Center at Tufts Medical Center, 260 Tremont Street, Floor 9–11, MA 02111, USA. e-mail: nadiakwaheed@gmail.com

Received: July 13, 2024
Accepted: January 30, 2025
Published: February 28, 2025

Keywords: retinal microaneurysm; diabetic retinopathy; macular edema; retinal blood flow; optical coherence tomography angiography

Citation: Takahashi H, Hwang Y, Won J, Jamil MU, Yaghy A, Liang MC, Baumal CR, Witkin AJ, Ohno-Matsui K, Duker JS, Fujimoto JG, Waheed NK. Evaluating blood flow speed in retinal microaneurysms secondary to diabetic retinopathy using variable interscan time analysis OCTA. Transl Vis Sci Technol. 2025;14(2):27, https://doi.org/10.1167/tvst.14.2.27

Purpose: To quantify the blood flow speed within retinal microaneurysms (MAs) and investigate the relationship between blood flow speed and clinical characteristics in eyes with diabetic retinopathy (DR).

Methods: Variable interscan time analysis (VISTA) quantifies blood flow speed in the vasculature by measuring how fast optical coherence tomography (OCT) angiography (OCTA) saturates for different interscan times. Macular OCTA imaging was performed in eyes with DR using a high-speed swept-source OCT prototype instrument operating at a 600-kHz A-scan rate. The presence of MAs was determined using OCT B-scans, and three-dimensional MA masks were generated. VISTA flow speed (VFS) was determined within MAs and the retinal capillary plexus (RCP). Intraluminal reflectivity, axial location within the RCP, and the presence of intraretinal fluid (IRF) around the MAs were evaluated.

Results: A total of 123 MAs were detected from 24 eyes of 20 patients with DR. Mean VFS was 1.26 ms^{-1} (95% confidence interval, 1.16–1.35). MAs with medium and high intraluminal reflectivity had slower VFS than those with low intraluminal reflectivity ($P < 0.01$) and often had slower VFS than the RCP ($P < 0.01$). Sixty-six MAs were located near IRF and had slower VFS than the other 57 MAs without surrounding IRF (1.16 ms^{-1} vs. 1.37 ms^{-1}; $P = 0.03$).

Conclusions: VISTA OCTA can assess blood flow speed of MAs in relation to other structural features in DR. Decreased blood flow speed in MAs is correlated with the presence of IRF around MAs.

Translational Relevance: We offer a new method that quantifies the blood flow speed of MAs to study the development of diabetic macular edema.

Introduction

Retinal microaneurysms (MAs), grape-like or spindle-shaped dilations of retinal capillaries, are a hallmark of diabetic retinopathy (DR).[1,2] Although MAs are the earliest clinical sign of DR, they can develop at any stage of DR. MAs can assume various shapes and internal structures even in the same eye, which makes it challenging to quantify and assess their role in DR pathogenesis.[3] Fluorescein angiography (FA) is a standard but invasive diagnostic procedure to evaluate MA and fluorescein leakage related to the accumulation of intraretinal fluid (IRF).[4–6]

The combination of optical coherence tomography (OCT) and OCT angiography (OCTA) can

assess the retinal capillary plexus and its abnormalities in three dimensions without requiring intravenous contrast.[7–14] On the other hand, Doppler OCT can directly measure blood flow velocity, but it is focused on the major retinal vessels, and the number of vessels that can be measured simultaneously is limited.[15–18] Other imaging technologies, such as scanning laser Doppler flowmetry (SLDF) and laser Doppler holography (LDH), can quantify flow in the retina.[19–24] However, SLDF and LDH are not depth resolved and not capable of distinguishing and evaluating retinal capillaries in different retinal layers.

Recent advances in ultra-high-speed swept-source lasers enable extensions of OCTA for hemodynamic assessment by acquiring more repeated B-scans with shorter interscan times. One example is variable interscan time analysis (VISTA), which characterizes blood flow speed by comparing short and long interscan time OCTA. Previous generation VISTA studies identified relatively slow blood flow speeds in MAs, intraretinal microvascular abnormalities, and neovascularization.[25–30] However, the flow speed information was qualitative, and quantitative measurement was not possible.

More recently, we developed a next-generation VISTA method, which quantifies blood flow speed by measuring the rate at which OCTA signals saturate versus interscan time.[31] This next-generation VISTA technique can detect subtle blood flow changes such as pulsatility in individual retinal capillaries and provides high repeatability for capillary blood flow speed measurements.

The purpose of this study is to assess blood flow speeds in individual MAs and correlate them with their clinical characteristics using swept-source OCT (SS-OCT) and next-generation VISTA OCTA. This study aims to comprehensively assess the hemodynamics and structure of MAs, as well as their associations with IRF.

Methods

Study Participants

Between January and December 2022, patients diagnosed with DR were enrolled in a prospective, observational study at the New England Eye Center, Tufts Medical Center, Boston, Massachusetts. This study was approved by the institutional review boards at Tufts Medical Center and Massachusetts Institute of Technology. The research adhered to the tenets of the Declaration of Helsinki and complied with the Health Insurance Portability and Accountability Act of 1996. Informed written consent was obtained from all patients before OCT imaging.

Patients underwent comprehensive ophthalmic examination, including measurement of best-corrected visual acuity (BCVA), intraocular pressure, slit-lamp biomicroscopy, and fundus examination. Visual acuity was measured using a Snellen chart and converted to logarithm of minimum angle of resolution (logMAR). The presence of diabetic macular edema (DME) was determined as a retinal thickness of 300 µm or more, either in the central subfield or a subfield quadrant directly adjacent to the central subfield with a diameter of 3 mm. Eyes with prior laser treatment and intravitreal anti–vascular endothelial growth factor (VEGF) injection within 1 month were excluded. Images with poor quality due to media opacity and poor fixation were also excluded.

SS-OCT Imaging and VISTA OCTA

The prototype SS-OCT system utilized a high-speed, micro-electromechanical systems–vertical cavity surface emitting laser and is described in our previous publication.[32] Table 1 summarizes the OCTA proto-

Table 1. Prototype Swept-Source OCT Angiography Protocols.

FOV	Fundamental Interscan Time, ms	Longest Interscan Time, ms	A-Scan Spacing, µm	B-Scan Repeats[a]	Scanner Duty Cycle	A-Scans/ B-Scan	B-Scans	Acquisition Time, S
3 × 3 mm	1	7	6.7	8	0.75	450	450	3.60
5 × 5 mm	1.25	5	8.8	5	0.76	570	570	3.57
6 × 6 mm	1.19	5.95	12	6	0.70	500	500	3.58

FOV, field of view.

[a]Scanning protocols with *N* B-scan repeats and the fundamental interscan time Δt (the interscan time between sequential B-scans) provide OCTA at Δt, $2\Delta t$, … $(N-1)\,\Delta t$.

cols used in the study. Blood flow speed quantification in MAs and retinal capillary plexus (RCP) was performed using the next-generation VISTA method.[31] In short, VISTA measures how fast OCTA saturates versus interscan time (the time between repeated B-scans) as a surrogate marker for blood flow speed. Fast blood flow results in a rapid OCTA saturation with increasing interscan time, while slow blood flow speed leads to a more gradual saturation. VISTA performs five or more repeated B-scans and computes OCTA signals at multiple interscan times, as modeled by $\mathrm{OCTA}(\tau) = \beta\ (1 - \exp\ (-\alpha\tau))$, to measure α, a surrogate for blood flow speed, the VISTA flow speed (VFS), and β, the saturated OCTA signal. Flow speed can be visualized using pseudo-colored en face OCTA images generated by mapping VFS to hue in an hue, saturation, and value (HSV) color map.

Retinal Layer Segmentation to Determine VISTA Flow Speed of Capillary Plexuses

Two RCP groups were assessed: superficial capillary plexus + intermediate capillary plexus (SCP + ICP) and deep capillary plexus (DCP). The SCP + ICP is between the posterior of the retinal nerve fiber layer and the middle of the inner nuclear layer (INL). The DCP is between the middle of the INL and 80 µm anterior to the retinal pigment epithelium. To compute the VFS in the SCP + ICP and DCP, a three-dimensional (3D) vessel mask for each plexus group was generated from OCTA, as described in our recent publication.[31] Vessels with diameters larger than 40 µm had saturated flow speeds and were excluded.

3D MA Mask Generation to Determine VISTA Flow Speed Within MAs

The 3D masks were generated for each MA (Fig. 1). First, a retinal specialist (HT) identified a cuboid that contained the MA using structural OCT volumes. Using this cuboid, three projected OCT images were generated by averaging the OCT intensity in three orthogonal directions. Then, the boundaries of the MA were manually traced on each projected image, and three two-dimensional (2D) masks were produced. These 2D masks were intersected within the cuboid to generate a 3D mask for the MA. This method using intersecting projections offers a more accurate representation of the MA than simpler geometric shapes like cuboids or spheres and is more practical than manual volume tracing. We note that only structural OCT, not OCTA, was used to identify and generate the 3D masks for MA. OCTA measurements in the 3D masks were used to evaluate VFS for each MA.

MA Categorization Based on Reflectivity, Axial Position, and Intraretinal Fluid

All MAs were classified into three groups (high, medium, and low) by a single grader (HT) according to internal OCT reflectivity, following a previous study.[33] The lumen of MAs was considered hyperreflective (high) if its OCT reflectivity was similar to that of the MA wall, hyporeflective (low) if it was similar to that of cystic intraretinal fluid, and moderate (medium) if the reflectivity was intermediate. Additionally, the uniformity of internal reflectivity was assessed (homogeneous, heterogeneous). If the reflectivity was consistent within an MA, it was classified as a homogeneous MA. Varying reflectivity within an MA was classified as heterogeneous.

The axial location (SCP + ICP, DCP) of each MA was determined using B-scan images. MAs anterior to the middle of the INL were classified as MAs located in the SCP + ICP, and MAs posterior to the middle of the INL were classified as MAs in the DCP. For MAs located in both the SCP + ICP and the DCP, OCT en face images at each depth (z-stack) were reviewed to determine the closest connection to the RCP.

The presence of IRF (IRF+, IRF−) was determined by two graders (HT and MUJ) using OCT B-scans and en face projections. If cystic fluid was observed within 250 µm from the center of an MA in the same capillary plexus, the MA was classified as IRF+. Otherwise, MAs were classified as IRF−. Discrepancies between the two graders were resolved through open adjudication.

Statistical Analysis

Statistical analysis was performed using SPSS Statistics software version 29.0.0.0 (IBM Corp, New York, NY, USA). Data are presented as mean ± standard deviation (SD) unless specified otherwise. When assessing the statistical significance of the differences between the groups, Student's *t*-tests and one-way analysis of variance (ANOVA) were performed after normal distributions were confirmed by Shapiro–Wilk tests. For data not following normal distributions, the Mann–Whitney *U* test and Kruskal–Wallis test were used. A *P* value less than 0.05 was considered significant.

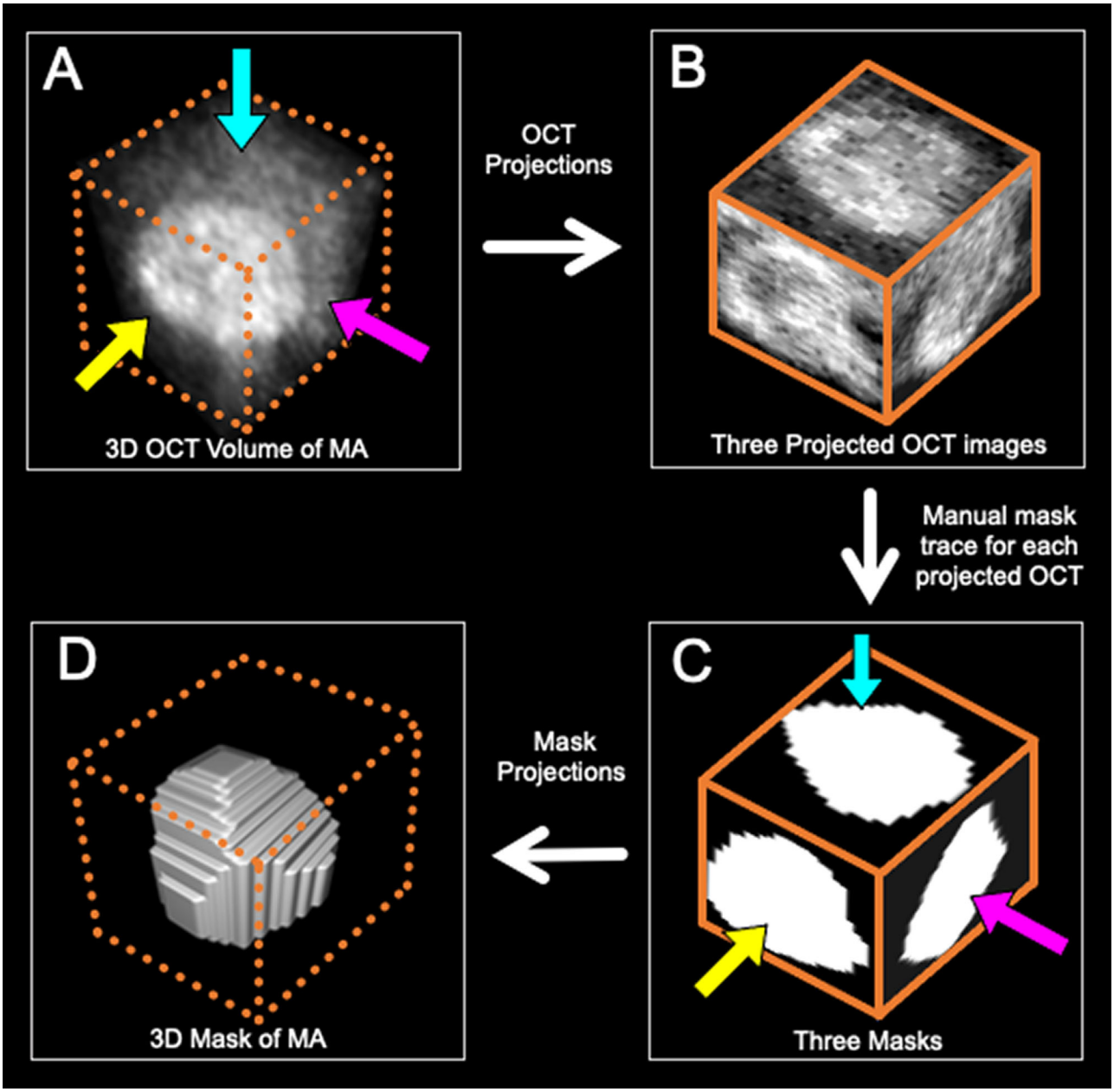

Figure 1. Method for generating a 3D mask of a retinal MA. (**A**) A cuboid box containing an MA is identified from the structural OCT volume. (**B**) Three en face images are generated by projecting the cuboid in three orthogonal directions. (**C**) Three 2D masks containing the microaneurysm are traced from the projected en face images. (**D**) The 3D mask is generated by intersecting the 2D masks.

Results

Twenty-four eyes from 20 patients with DR were included in the study. The mean age of the study participants was 58 ± 14 (range, 31–79) years. The mean logMAR visual acuity was 0.30 ± 0.39 (Snellen = 20/41). Of these 24 eyes, 9 eyes were classified as mild nonproliferative diabetic retinopathy (NPDR), 5 eyes as moderate NPDR, 3 eyes as severe NPDR, and the remaining 7 eyes as proliferative diabetic retinopathy (PDR). Macular edema was present in 13 (54%) DR eyes. The clinical characteristics of DR eyes are summarized in Table 2. The 13 eyes with DME had worse BCVA and a larger central subfield retinal thickness than the 11 eyes without DME. The median number of retinal MAs in DME eyes was more than those in eyes without DME (6 vs. 2; $P = 0.04$, Mann–Whitney U test) over a 5-mm × 5-mm or 6-mm × 6-mm field of view. The mean VFS of MAs, $(\text{SCP} + \text{ICP})^{\text{VFS}}$, and DCP^{VFS} was not different between DR eyes with and without DME.

Table 2. Clinical Characteristics of Patients With DR With and Without DME

Characteristic	DME Present	DME Absent	*P* Value
Patient characteristics			
Number of patients	12	8	
Mean age in years	61 ± 11	54 ± 17	0.27[a]
Male gender	9 (69)	8 (73)	0.85[b]
Race			
Caucasian	8 (67)	5 (62)	
African American	3 (25)	2 (25)	0.78[b]
Asian	1 (8)	1 (13)	
Type 2 DM	11 (85)	8 (73)	0.63[b]
Serum HbA1c %	8.0 ± 1.5	7.9 ± 1.3	0.87[a]
Insulin dependency Ocular characteristics	12 (80)	7 (64)	0.66[b]
Number of eyes	13	11	
Prior intravitreal anti-VEGF treatment	6 (46)	5 (45)	0.97[b]
Prior laser photocoagulation[c]	3 (23)	3 (27)	0.81[b]
BCVA in logMAR units (Snellen)	0.48 ± 0.44 (20/60)	0.06 ± 0.11 (20/23)	<0.01[a]
DR classification			
Mild NPDR	4 (31)	5 (46)	
Moderate NPDR	2 (15)	3 (27)	0.35[b]
Severe NPDR	3 (23)	0 (0)	
PDR	4 (31)	3 (27)	
DME location			
Foveal only	8 (62)		
At the perifovea	4 (31)		
Both	1 (7)		
CST, microns	341 ± 96	262 ± 36	0.01[a]
Retinal microaneurysm			
Median,[d] *n*	6	2	0.04[e]
VISTA flow speed (ms^{-1})	1.29 ± 0.56	1.18 ± 0.47	0.35[a]
Superficial and intermediate capillary plexus, VISTA flow speed (ms^{-1})	1.84 ± 0.34	1.72 ± 0.28	0.34[a]
Deep capillary plexus, VISTA flow speed (ms^{-1})	1.56 ± 0.30	1.50 ± 0.25	0.82[a]

Values are presented as *n* (%) or mean ± standard deviation unless otherwise indicated. CST, central subfield thickness; DM, diabetes mellitus; PDR, proliferative diabetic retinopathy.

[a]Student's *t*-test.

[b]χ^2 test.

[c]All laser treatments were performed with pan-retinal photocoagulation.

[d]Number of retinal microaneurysms was compared between 12 eyes with DME and 10 eyes without DME, which were examined with a scanning field of either 5 × 5 mm or 6 × 6 mm.

[e]Mann–Whitney *U* test.

A total of 123 MAs were detected on OCT B-scans of 24 patients with DR (Figs. 2 and 3). The mean VFS of MAs was 1.26 ± 0.53 ms^{-1}. The mean largest linear diameter and volume of the MAs were 132.8 ± 37.7 µm and (7.87 ± 6.26) × 10^5 $µm^3$, respectively, as measured from the 3D MA masks. The largest linear diameter and volume of the MAs were not correlated with the VFS in univariate regression analysis (P = 0.30 and 0.34, respectively).

Of 123 MAs, 36 MAs were classified as hyperreflective (high reflectivity), 55 MAs as moderate-reflective (medium reflectivity), and the remaining 32 MAs as hyporeflective (low reflectivity). The mean VFS of moderate and hyperreflective MAs were slower than those of hyporeflective MAs (1.19 ± 0.34 and 1.14 ± 0.42 ms^{-1} vs. 1.52 ± 0.79 ms^{-1}; P < 0.01, one-way ANOVA) (Fig. 4A), whereas MA diameters (122.2 ± 38.6, 136.3 ± 35.3, and 136.9 ± 40.1 µm; in the low,

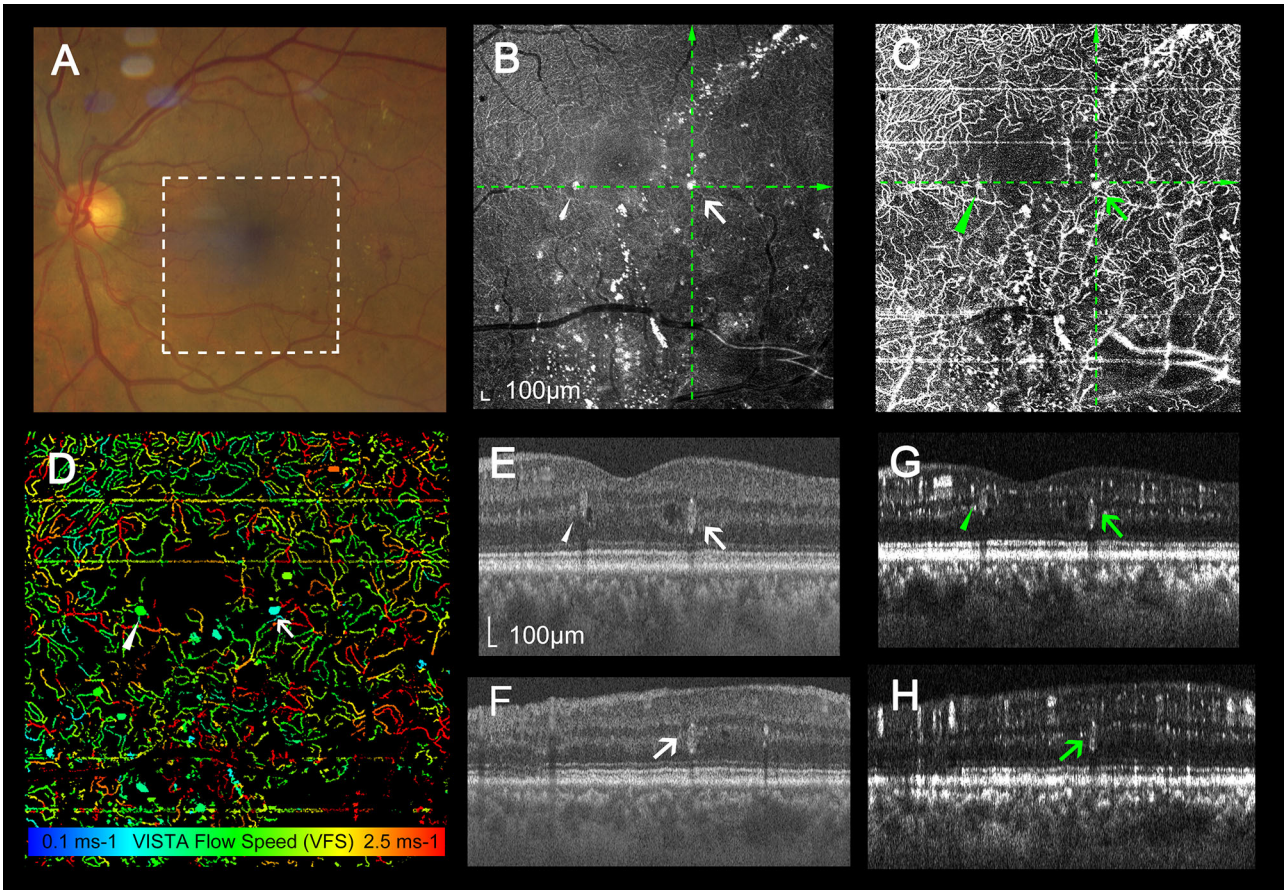

Figure 2. Multimodal imaging of a 66-year-old patient with mild nonproliferative diabetic retinopathy in the left eye imaged by high-speed, swept-source OCT. (**A**) Color fundus image shows dot and blot hemorrhages temporal to the fovea. A *white rectangle* highlights the area corresponding to images (**B**), (**C**), and (**D**) and is slightly cropped from the scanned region. (**B**) En face OCT image shows MAs with hyperreflectivity (*white arrow* and *arrowhead*). The *green dotted bars* indicate the location of the OCT B-scans. *White bar*: 100 µm. (**C**) En face OCTA image shows knob-like MAs in the DCP (*green arrow* and *arrowheads*). (**D**) En face VISTA OCTA image shows colored MAs and the DCP. VFS of MAs was measured as 1.27 ms^{-1} (*white arrowhead*) and 0.79 ms^{-1} (*white arrow*), which were slower than the mean VFS of the DCP (1.58 ms^{-1}). (**E**) A horizontal B-scan image shows MAs with high and heterogeneous intraluminal reflectivity in the DCP (*white arrow* and *arrowhead*). Both MAs have directly adjacent IRF. (**F**) A vertical B-scan image shows MA in the DCP (*white arrow*). (**G**) A horizontal cross-sectional OCTA image shows MAs (*green arrow* and *arrowheads*). (**H**) A vertical cross-sectional OCTA image shows an MA posterior to the inner nuclear layer (*green arrow*).

medium, and high reflectivity groups, respectively) and volume (6.85 ± 6.28, 8.41 ± 6.49, and 7.96 ± 6.02 × 10^5 μm^3; in the low, medium, and high reflectivity groups, respectively) were not statistically different. Of all 123 MAs, 51 MAs (41%) were classified as homogeneous and the other 72 were heterogeneous. The mean VFS of heterogenous MAs was slower than those of homogeneous MAs (1.16 ± 0.39 vs. 1.40 ± 0.67 ms^{-1}; $P = 0.03$) (Fig. 4B), whereas the diameter (137.7 ± 37.3 vs. 125.9 ± 38.0 µm) and volume (8.08 ± 6.44 vs. 7.58 ± 6.10 × 10^5 μm^3) were not significantly different. The distribution of MAs classified using intraluminal reflectivity and homogeneity is shown in Figure 4C. The mean VFS of MAs with low homogeneous reflectivity was faster than the other groups of MAs ($P < 0.001$, one-way ANOVA) (Fig. 4D).

A total of 55 MAs (45%) were located near the SCP + ICP, and the other 68 MAs (55%) were located near the DCP. There was no significant difference in VFS between MAs in the SCP + ICP versus those in the DCP (1.17 ± 0.39 vs. 1.33 ± 0.62 ms^{-1}; $P = 0.11$) (Fig. 5A). Figure 5B shows that MA^{VFS}(VFS of MA) was slower than both $(SCP + ICP)^{VFS}$ and DCP^{VFS} in 103 MAs (group 1; 84%), slower than $(SCP + ICP)^{VFS}$ but not DCP^{VFS} in 7 MAs (group 2; 6%), and greater than $(SCP + ICP)^{VFS}$ and DCP^{VFS} in the remaining 13 MAs (group 3; 10%). This relative relationship of VFS between MAs and RCP was associated with the intralumi-

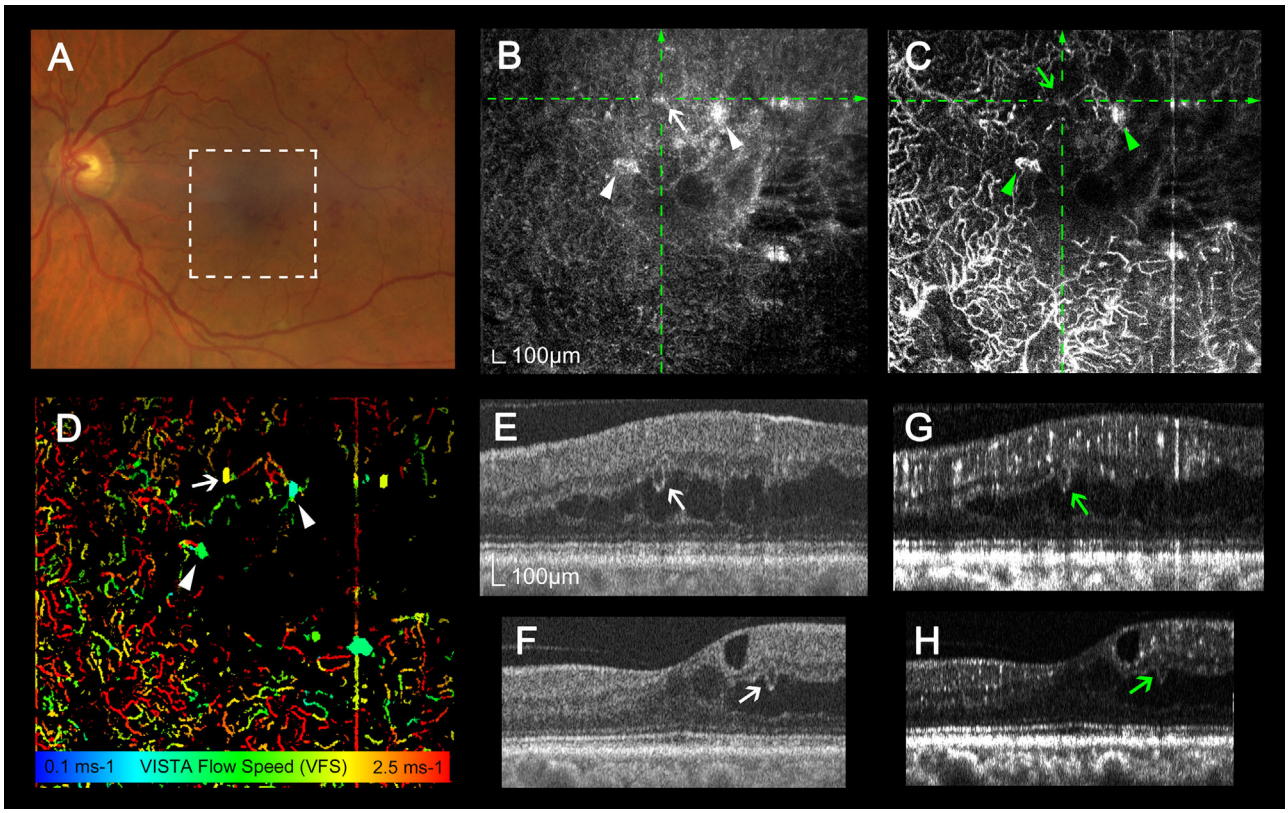

Figure 3. Multimodal imaging of a 65-year-old patient with severe nonproliferative diabetic retinopathy. (**A**) Color fundus image of the left eye shows multiple blot hemorrhages in the temporal paramacular area. A *white rectangle* indicates the area corresponding to images (**B**), (**C**), and (**D**) and is slightly cropped from the scanned OCT region. (**B**) En face OCT image shows MAs with hyperreflectivity (*white arrowheads* and *white arrow*). The *green dotted bars* indicate B-scan OCT locations. *White bar*: 100 µm. (**C**) En face OCTA image shows MAs (*green arrowheads*). The MA indicated by *white arrows* in (**B**) is not clearly visualized on this image because of low OCTA signal (*green arrow*). (**D**) En face VISTA OCTA shows colored MAs and the DCP. The VFS of the MA (*white arrow*) was measured as 1.91 ms^{-1}, which was slower than the 2.07 ms^{-1} mean VFS of the DCP. This MA has faster blood flow speed than other two MAs (*white arrowheads*, *left*; 1.15 ms^{-1}, *right*; 0.85 ms^{-1}). (**E**) A horizontal B-scan OCT shows an MA with low homogeneous intraluminal reflectivity in the DCP (*white arrow*). (**F**) A vertical B-scan image shows an MA in the DCP (*white arrow*). The MAs have adjacent intraretinal fluid beside them. (**G**) A horizontal B-scan OCTA image shows an MA (*green arrow*). (**H**) A vertical B-scan OCTA image shows low OCTA signal at the area of the MA (*green arrow*).

nal reflectivity of the MAs ($P < 0.01$, χ^2 test) (Fig. 5C).

The two graders determined the presence of surrounding IRF near MAs with an agreement of 68% (84 MAs). A concordance index κ of 0.63 (95% confidence interval, 0.52–0.74) was obtained, indicating a moderate level of agreement. After reaching consensus through open adjudication, a total of 66 MAs (54%) were classified into the IRF+ group and the remaining 57 MAs into the IRF– group. The mean VFS of MAs in the IRF+ group was slower than MAs in the IRF– group (VFS 1.15 ± 0.04 ms^{-1} vs. 1.37 ± 0.09 ms^{-1}, $P = 0.03$). The intraluminal reflectivity, homogeneity of reflectivity, proximity to SCP + ICP or DCP, largest linear diameter, and volume of MAs were not statistically different between the two groups (Table 3).

Discussion

In this study, we quantitatively examined blood flow speed of MAs and RCP in patients with DR using VISTA OCTA. MAs originate from RCP, in which blood perfusion is closely associated with the high metabolic demands of the retina.[14,34] Therefore, hemodynamic information from VISTA OCTA may provide insights into subclinical alterations of retinal circulation, which are not readily available from standard OCTA. Furthermore, utilizing structural information of individual MAs from dense OCT volume scans, we investigated the relationships between the blood flow speeds and clinically relevant parameters, such as largest linear diameter,[35,36] volume, axial location,[37] and intraluminal reflectivity[33,38] of MAs, as well as the presence of surrounding IRF.

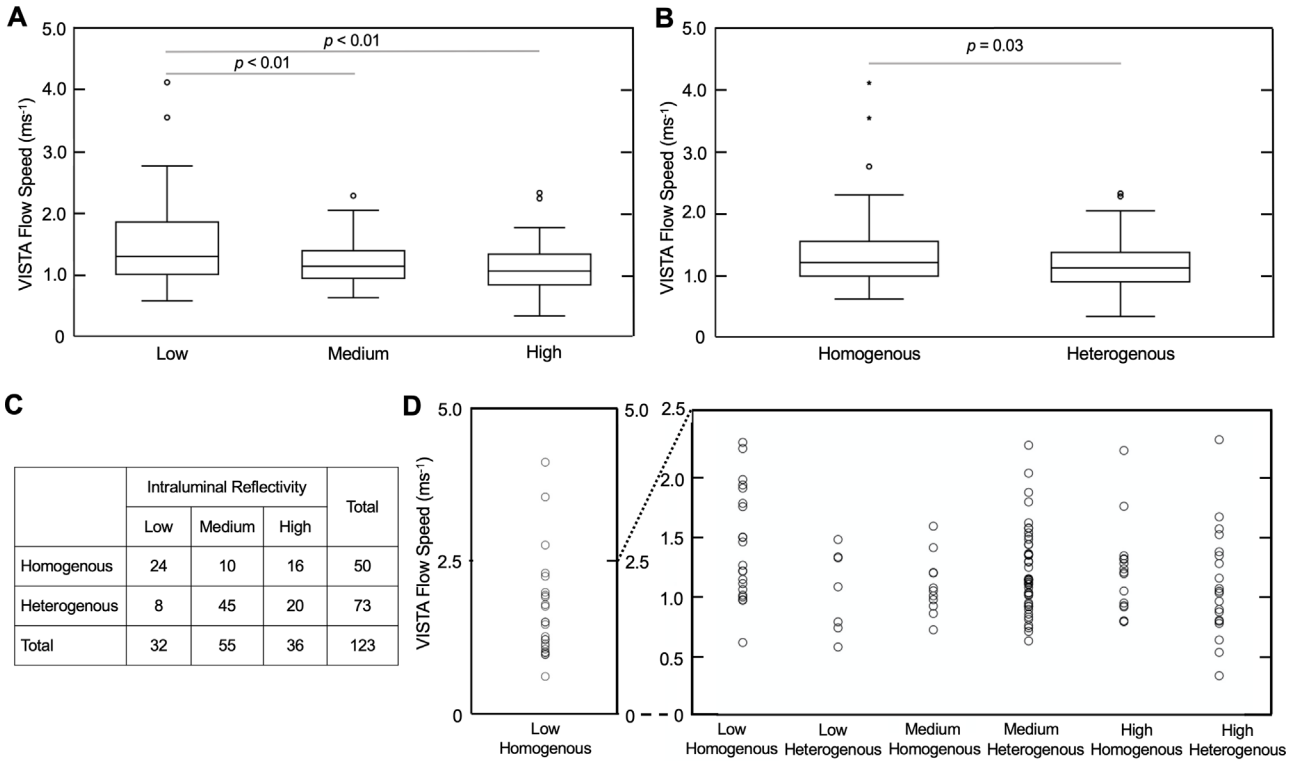

	Intraluminal Reflectivity			Total
	Low	Medium	High	
Homogenous	24	10	16	50
Heterogenous	8	45	20	73
Total	32	55	36	123

Figure 4. VFS of retinal MAs in diabetic retinopathy. (**A**) Box plots showing VFS of MAs versus intraluminal reflectivity of each MA. (**B**) Box plots of VFS of MAs versus homogeneity of intraluminal reflectiveness of each MA. (**C**) Distribution of MAs ($N = 123$) by intraluminal reflectivity and homogeneity. (**D**) VFS of MAs versus intraluminal reflectivity and homogeneity of each MA.

The mean largest linear diameter of MAs was 132.8 ± 37.7 µm with a range from 53.7 to 254.6 µm. The mean diameter of MAs measured using adaptive optics scanning laser ophthalmoscopy (AOSLO)[39] and adaptive optics OCT[40,41] was reported as 49 to 105 µm and 109 to 137 µm, respectively, which is consistent with our measurements using OCT. Although OCT does not achieve the high transverse resolution of adaptive optics, it has a wider field of view.

Recent studies investigated varying intraluminal reflectivity of MAs using OCT.[33,38] Utilizing a total of 145 MAs from 16 patients with DR, it was reported that MAs with medium and high intraluminal reflectivity were more clearly visualized in OCTA than MAs with low intraluminal reflectivity, suggesting a wide range of blood flow speeds associated with reflectivity of MAs.[33] One study observed MAs with varying reflectivity in patients with NPDR over 1 year and showed that extracellular fluid developed more around hyperreflective MAs than hyporeflective MAs.[38]

As shown in Figures 3B and 3C, hyporeflective MAs may appear as having "no signal" in OCT images due to the selected brightness settings chosen for the printed image, which are optimized to display the overall retina but may fail to reveal OCT signals within MAs. The actual OCT intensity is significant relative to the background, and thus VISTA can measure flow speed in these hyporeflective MAs.

Similarly, our results show MAs with heterogeneous intraluminal reflectivity had slower blood flow speed than MAs with homogeneous intraluminal reflectivity, suggesting the existence of different materials within MAs that may be associated with slower blood flow speed. A previous histologic study showed that intraluminal materials in MAs can consist of accumulated red blood cells, monocytes, polymorphonuclear cells, macrophages, lipid depositions, and thickened basement membranes of vascular endothelial cells, which can generate heterogeneous optical scattering properties.[42] In addition, these intraluminal hyperreflective materials may change over time, as reported by Hafner et al.[40] using adaptive optics OCT. In our study, we believe that the intraluminal materials may behave like static components (compared to moving red blood cells) within the MA during image acquisition, decreasing the VFS of the MA. Moreover, MAs with higher flow speeds may cause the speckle pattern to become decorrelated across repeated OCT scans. When these B-scans are averaged to produce the structural OCT image, the decor-

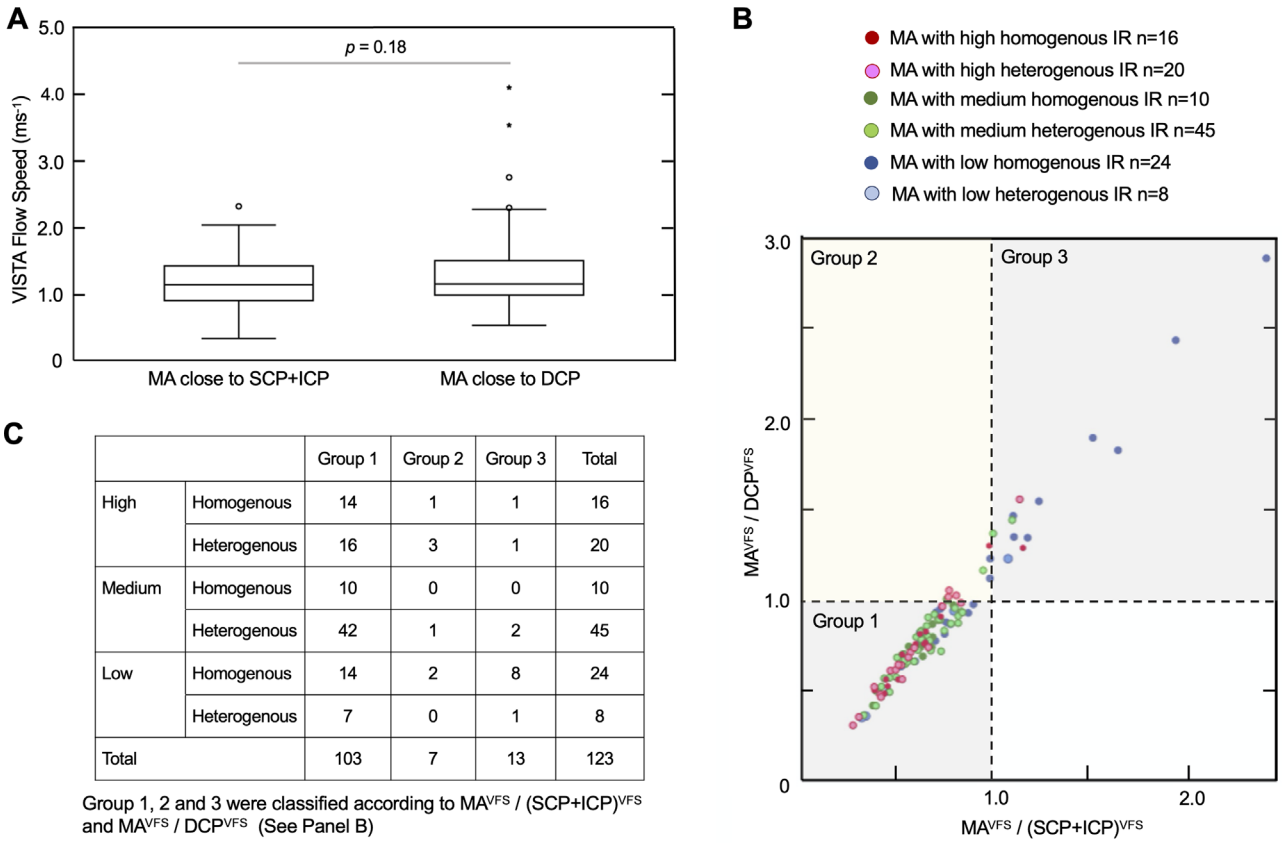

		Group 1	Group 2	Group 3	Total
High	Homogenous	14	1	1	16
	Heterogenous	16	3	1	20
Medium	Homogenous	10	0	0	10
	Heterogenous	42	1	2	45
Low	Homogenous	14	2	8	24
	Heterogenous	7	0	1	8
Total		103	7	13	123

Group 1, 2 and 3 were classified according to MA^{VFS} / $(SCP+ICP)^{VFS}$ and MA^{VFS} / DCP^{VFS} (See Panel B)

Figure 5. VFS of retinal MAs in diabetic retinopathy. (**A**) Box plots showing VFS of MAs versus axial location of each MA. (**B**) Scatterplot of the ratio MA^{VFS}/DCP^{VFS} versus the ratio $MA^{VFS}/(SCP + ICP)^{VFS}$. (**C**) Distribution of MAs ($N = 123$) by intraluminal reflectivity and classification according to the ratio MA^{VFS}/DCP^{VFS} and the ratio $MA^{VFS}/(SCP + ICP)^{VFS}$.

relation may result in a homogeneous intraluminal reflectivity.

As expected, most MAs (84%) had blood flow speed slower than the SCP + ICP and DCP, and blood flow speeds between MAs in the SCP + ICP versus in the DCP were not statistically different. Li et al.[43] simulated flow velocity in MAs using AOSLO and platelet aggregation models and demonstrated that flow speed is slower in MAs than in the feeding and draining vessels. This may explain our observation of slower blood flow speed within MAs than mean blood flow speed of both SCP + ICP and DCP (group 1), the most common case (84%) in our study. On the other hand, we did not evaluate the shape of each MA and the distance between MAs and draining vessels, and this could have introduced a large variance in the VFS of MAs.

It is also important to highlight that the blood flow speed of MAs having surrounding IRF was slower than those without surrounding IRF, whereas the other parameters (intraluminal reflectivity, axial location, and largest linear diameter) were not different between the MAs with and without adjacent IRF. Recently, Gao et al.[44] also categorized MAs into three groups based on their perfusion status. To investigate the relationship between perfusion status and VISTA flow speed, we applied the same classification method as Gao et al.[44] by categorizing MAs into nonperfused, partially perfused, and fully perfused groups using OCTA B-scans. Figure 6A presents representative MAs from each category. Of the 123 MAs, 12% were classified as nonperfused, 55% as partially perfused, and 33% as fully perfused. We compared VISTA flow speed across these groups (Fig. 6B), which showed significant differences (Kruskal–Wallis test, $P = 0.0057$). Post hoc Mann–Whitney U tests revealed statistically significant differences between fully perfused versus partially perfused MAs, as well as fully perfused versus nonperfused MAs ($P = 0.0059$ and $P = 0.0104$, respectively) but not between partially perfused and nonperfused MAs ($P = 0.312$).

Fully perfused MAs exhibited higher flow speeds than partially perfused MAs, likely because partially perfused MAs may contain intraluminal materials that

Table 3. Comparison of Characteristics and VISTA Flow Speed Among Retinal Microaneurysms With and Without Surrounding Intraretinal Fluid

Characteristic	IRF Present	IRF Absent	*P* Value
Number of microaneurysms	66	57	
Intraluminal reflectivity			
High	13 (20)	19 (33)	0.16[a]
Medium	34 (52)	21 (36)	
Low	19 (28)	17 (30)	
Homogeneity of intraluminal reflectivity			
Homogeneous	23 (35)	28 (49)	0.14[a]
Heterogeneous	43 (65)	29 (51)	
Axial location			
At SCP and ICP	29 (44)	30 (53)	0.37[a]
At DCP	37 (56)	27 (47)	
Largest diameter (µm), mean ± SD	136.1 ± 38.1	129.0 ± 37.6	0.30[b]
Volume (μm^3), mean ± SD	8.52 ± 6.79	7.12 ± 5.61	0.22[b]
VISTA flow speed (ms^{-1}), mean ± SD	1.15 ± 0.35	1.37 ± 0.67	0.03[b]

Values are presented as *n* (%) or mean ± standard deviation unless otherwise indicated.
[a] χ^2 test.
[b] Student's *t*-test.

increase fluid resistance, thereby reducing flow speed. Notably, nonperfused MAs still showed nonzero VFS values. This is consistent with our expectations because our OCTA system uses interscan times that are two to five times shorter than those in commercial OCTA systems. These shorter interscan times can result in weaker OCTA signals for MAs with slower flow due to limited red blood cell displacement within each interval. However, VISTA measures flow speed based on the rate at which OCTA signals saturate over multiple interscan time points rather than relying solely on OCTA signal intensity, allowing it to detect slow flow speeds even in MAs with low OCTA signals.

Limitations of this study include the small number of enrolled patients, cross-sectional design, and lack of longitudinal follow-up. About half of the eyes with DR have a history of anti-VEGF treatment or prior laser photocoagulation, which may have affected the VFS in eyes with DR and the amount of IRF in eyes with DME in our study. A longitudinal study with a larger sample number is needed to better understand the correlation of MA flow speeds with clinical features and treatment outcomes.

We note that blood flow speeds in MAs are modulated by cardiac pulsatility, similar to retinal capillaries. Therefore, the VFS measurements in this study are subject to pulsatility effects. However, because the cardiac phase during imaging is random for each MA, the effect of pulsatility on VFS can be treated as an error term, introducing variance but not bias. This may reduce the statistical power of our analyses. To obtain pulsatility-averaged VFS measurements, OCTA images can be acquired at different cardiac phases.[45] However, this approach will require multiple image acquisitions and OCT system integration with a pulse oximeter, significantly increasing acquisition time and system complexity.

Three different scanning protocols were used, and the differences in scan density may have affected the measured volume of MAs. However, our recent study showed that VFS measurements were compatible between different imaging protocols.[31] Figure 1 shows a method for generating a 3D MA mask from three 2D masks. While this approach offers a time-efficient way to create a 3D mask, it is expected to overestimate the MA volume by approximately 10% to 12% and length by 3% to 4%. More advanced techniques, such as binary tomography and voxel carving, could improve 3D mask accuracy using projections.[46,47] Additionally, deep learning approaches have been effective in identifying MAs from 2D images in various imaging modalities and may enable fully automated 3D MA segmentation in OCT without the need for human readers or projections.[48,49]

The clinical relevance of measuring MA hemodynamics remains an open question, as in vivo studies are still at an early stage. To the best of our knowledge, this study represents the first in vivo measurement of MA hemodynamics in humans. MA hemodynamic markers, such as blood flow velocity and shear stress,

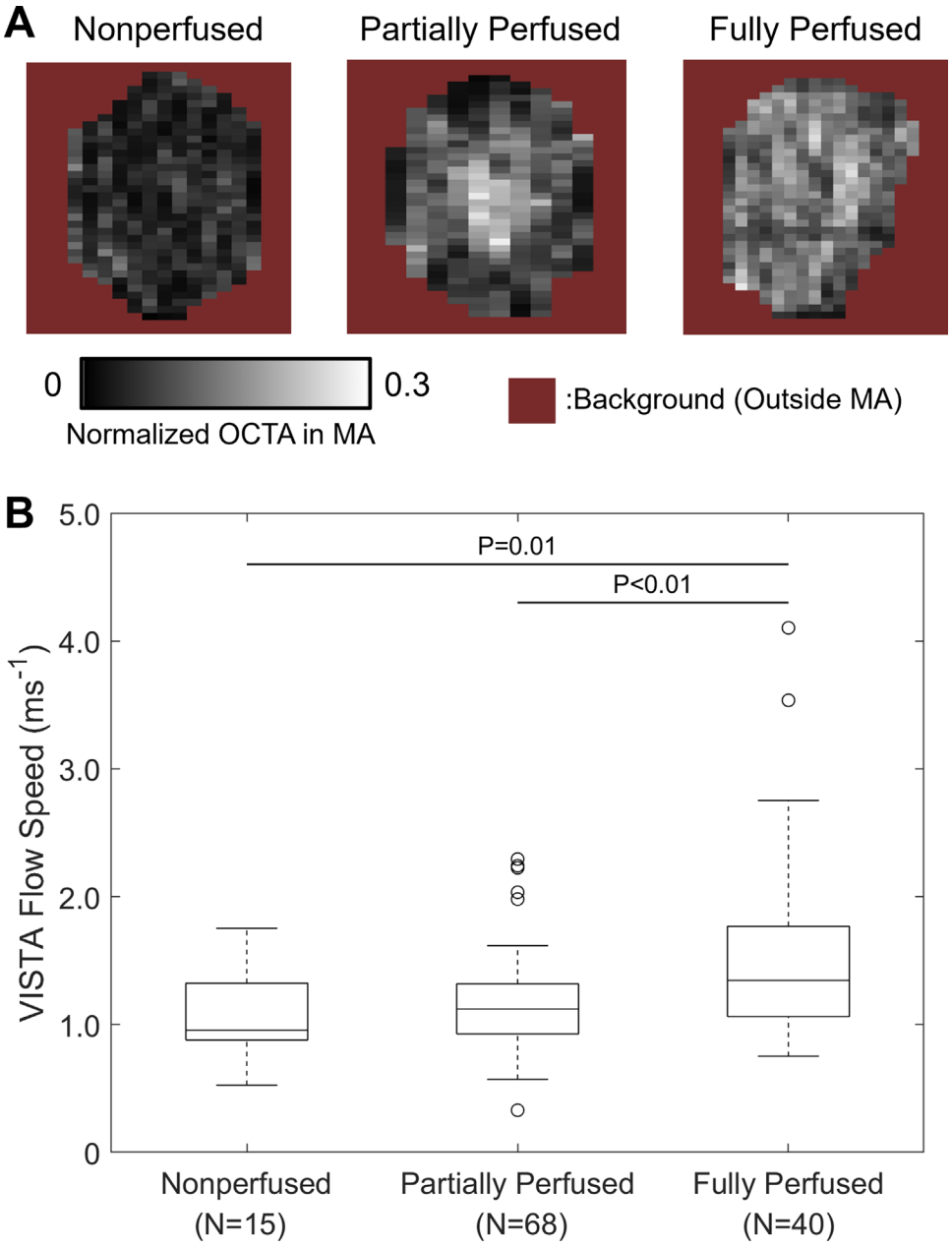

Figure 6. Perfusion status of retinal MAs versus VFS. (**A**) Representative OCTA B-scan images of MAs with different perfusion status: nonperfused (*left*), partially perfused (*middle*), and fully perfused (*right*). (**B**) Box plots showing VFS across the three perfusion status categories.

may provide insights into vascular wall integrity and thrombosis.[50] Compromised vascular walls can lead to MA leakage and retinal edema with DR progression.[51,52]

Previous studies have primarily relied on simulations or in vitro models to explore MA hemodynamics. For example, adaptive optics-based models have been used to calculate shear rates, microfluidic platforms have demonstrated reduced shear stress in larger MAs, and particle-based models have shown the relationship between flow speed and platelet aggregation.[53–55] In contrast, our study measures a surrogate marker for blood flow speed in vivo, providing a complementary approach to these earlier approaches.

In summary, in vivo measurements of blood flow speed of MAs and the RCP were performed in a single acquisition using high-speed SS-OCT and VISTA OCTA. The capability of assessing blood flow speed over multi-millimeter fields of view may help

develop quantitative OCTA biomarkers that can be used to better understand DR pathogenesis, including accumulation of fluid within the retinal inner layers.

Acknowledgments

Supported by the National Institutes of Health R01EY011289 and R01EY034080.

Disclosure: **H. Takahashi**, None; **Y. Hwang**, None; **J. Won**, None; **M.U. Jamil**, None; **A. Yaghy**, Beacon Therapeutics (C); **M.C. Liang**, Beacon Therapeutics (C), Genentech (C); **C.R. Baumal**, Apellis (E), EyePoint Pharma (C), Genentech (C), Ocuphire (C), Ophthea (C), Ora (C); **A.J. Witkin**, Apellis (F), Genentech (F); **K. Ohno-Matsui**, Santen (C), Cooper vision (C), Topcon (C), Eye Rising (C); **J.S. Duker**, EyePoint Pharma (E); **J.G. Fujimoto**, Optovue (I, P), Topcon (F), VISTA-OCTA (P); **N.K. Waheed**, Zeiss (F), Topcon (C, F), Nidek (C, F), Regeneron (F), Complement Therapeutics (C), OliX Pharmaceuticals (C), Iolyx Pharmaceuticals (C, I), Boehringer Ingelheim (C), Jansen (C), Ocular Therapeutix (C, E), Valitor (I), Ocudyne (I), Beacon Therapeutics (I)

References

1. Friedenwald JS. Diabetic retinopathy. *Am J Ophthalmol*. 1950;33(8):1187–1199.
2. Cogan DG, Toussaint D, Kuwabara T. Retinal vascular patterns. IV. Diabetic retinopathy. *Arch Ophthalmol*. 1961;66:366–378.
3. Garner A. Histopathology of diabetic retinopathy in man. *Eye (Lond)*. 1993;7:250–253.
4. Kwiterovich KA, Maguire MG, Murphy RP, et al. Frequency of adverse systemic reactions after fluorescein angiography. Results of a prospective study. *Ophthalmology*. 1991;98(7):1139–1142.
5. Kalogeromitros DC, Makris MP, Aggelides XS, et al. Allergy skin testing in predicting adverse reactions to fluorescein: a prospective clinical study. *Acta Ophthalmol*. 2011;89(5):480–483.
6. Kornblau IS, El-Annan JF. Adverse reactions to fluorescein angiography: a comprehensive review of the literature. *Surv Ophthalmol*. 2019;64(5):679–693.
7. Horii T, Murakami T, Nishijima K, Sakamoto A, Ota M, Yoshimura N. Optical coherence tomographic characteristics of microaneurysms in diabetic retinopathy. *Am J Ophthalmol*. 2010;150(6):840–848.
8. Couturier A, Mané V, Bonnin S, et al. Capillary plexus anomalies in diabetic retinopathy on optical coherence tomography angiography. *Retina*. 2015;35(11):2384–2391.
9. Ishibazawa A, Nagaoka T, Takahashi A, et al. Optical coherence tomography angiography in diabetic retinopathy: a prospective pilot study. *Am J Ophthalmol*. 2015;160(1):35–44.e1.
10. Hasegawa N, Nozaki M, Takase N, Yoshida M, Ogura Y. New insights into microaneurysms in the deep capillary plexus detected by optical coherence tomography angiography in diabetic macular edema. *Invest Ophthalmol Vis Sci*. 2016;57(9):348–355.
11. Nakao S, Yoshida S, Kaizu Y, et al. Microaneurysm detection in diabetic retinopathy using OCT angiography may depend on intramicroaneurysmal turbulence. *Ophthalmol Retina*. 2018;2(11):1171–1173.
12. Spaide RF, Fujimoto JG, Waheed NK, Sadda SR, Staurenghi G. Optical coherence tomography angiography. *Prog Retin Eye Res*. 2018;64:1–55.
13. Kaizu Y, Nakao S, Wada I, et al. Microaneurysm imaging using multiple en face OCT angiography image averaging: morphology and visualization. *Ophthalmol Retina*. 2020;4(2):175–186.
14. Waheed NK, Rosen RB, Jia Y, et al. Optical coherence tomography angiography in diabetic retinopathy. *Prog Retin Eye Res*. 2023;97:101206.
15. Miura M, Hong YJ, Yasuno Y, Muramatsu D, Iwasaki T, Goto H. Three-dimensional vascular imaging of proliferative diabetic retinopathy by Doppler optical coherence tomography. *Am J Ophthalmol*. 2015;159(3):528–538.
16. Tayyari F, Khuu LA, Flanagan JG, Singer S, Brent MH, Hudson C. Retinal blood flow and retinal blood oxygen saturation in mild to moderate diabetic retinopathy. *Invest Ophthalmol Vis Sci*. 2015;56(11):6796–6800.
17. Fondi K, Wozniak PA, Howorka K, et al. Retinal oxygen extraction in individuals with type 1 diabetes with no or mild diabetic retinopathy. *Diabetologia*. 2017;60(8):1534–1540.
18. Lee B, Novais EA, Waheed NK, et al. En face Doppler optical coherence tomography measurement of total retinal blood flow in diabetic retinopathy and diabetic macular edema. *JAMA Ophthalmol*. 2017;135(3):244–251.
19. Michelson G, Welzenbach J, Pal I, Harazny J. Automatic full field analysis of perfusion

images gained by scanning laser Doppler flowmetry. *Br J Ophthalmol*. 1998;82(11):1294–1300.
20. Nagaoka T, Kitaya N, Sugawara R, et al. Alteration of choroidal circulation in the foveal region in patients with type 2 diabetes. *Br J Ophthalmol*. 2004;88(8):1060–1063.
21. Lorenzi M, Feke GT, Cagliero E, et al. Retinal haemodynamics in individuals with well-controlled type 1 diabetes. *Diabetologia*. 2008;51(2):361–364.
22. Jung S, Kolwelter J, Bosch A, et al. Hypertrophic remodelling of retinal arterioles in patients with congestive heart failure. *ESC Heart Fail*. 2021;8(3):1892–1900.
23. Bosch A, Scheppach JB, Harazny JM, et al. Retinal capillary and arteriolar changes in patients with chronic kidney disease. *Microvasc Res*. 2018;118:121–127.
24. Puyo L, Paques M, Atlan M. Retinal blood flow reversal quantitatively monitored in out-of-plane vessels with laser Doppler holography. *Sci Rep*. 2021;11(1):17828.
25. Choi W, Moult EM, Waheed NK, et al. Ultrahigh-speed, swept-source optical coherence tomography angiography in nonexudative age-related macular degeneration with geographic atrophy. *Ophthalmology*. 2015;122(12):2532–2544.
26. Ploner SB, Moult EM, Choi W, et al. Toward quantitative optical coherence tomography angiography: visualizing blood flow speeds in ocular pathology using variable interscan time analysis. *Retina*. 2016;36:S118–S126.
27. Rebhun CB, Moult EM, Novais EA, et al. Polypoidal choroidal vasculopathy on swept-source optical coherence tomography angiography with variable interscan time analysis. *Transl Vis Sci Technol*. 2017;6(6):4.
28. Rebhun CB, Moult EM, Ploner SB, et al. Analyzing relative blood flow speeds in choroidal neovascularization using variable interscan time analysis OCT angiography. *Ophthalmol Retina*. 2018;2(4):306–319.
29. Arya M, Filho MB, Rebhun CB, et al. Analyzing relative flow speeds in diabetic retinopathy using variable interscan time analysis OCT angiography. *Ophthalmol Retina*. 2021;5(1):49–59.
30. Kaizu Y, Nakao S, Soda T, et al. Longer interscan times in OCT angiography detect slower capillary flow in diabetic retinopathy. *Ophthalmol Sci*. 2022;2(3):100181.
31. Hwang Y, Won J, Yaghy A, et al. Retinal blood flow speed quantification at the capillary level using temporal autocorrelation fitting OCTA. *Biomed Opt Express*. 2023;14(6):2658–2677.
32. John DD, Burgner CB, Potsaid B, et al. Wideband electrically-pumped 1050 nm MEMS-tunable VCSEL for ophthalmic imaging. *J Lightwave Technol*. 2015;33(16):3461–3468.
33. Parravano M, De Geronimo D, Scarinci F, et al. Diabetic microaneurysms internal reflectivity on spectral-domain optical coherence tomography and optical coherence tomography angiography detection. *Am J Ophthalmol*. 2017;179:90–96.
34. Puro DG. Retinovascular physiology and pathophysiology: new experimental approach/new insights. *Prog Retin Eye Res*. 2012;31(3):258–270.
35. An D, Tan B, Yu DY, Balaratnasingam C. Differentiating microaneurysm pathophysiology in diabetic retinopathy through objective analysis of capillary nonperfusion, inflammation, and pericytes. *Diabetes*. 2022;71(4):733–746.
36. Balaratnasingam C, An D, Hein M, Yu P, Yu DY. Studies of the retinal microcirculation using human donor eyes and high-resolution clinical imaging: insights gained to guide future research in diabetic retinopathy. *Prog Retin Eye Res*. 2023;94:101134.
37. Hasegawa N, Nozaki M, Takase N, Yoshida M, Ogura Y. New insights into microaneurysms in the deep capillary plexus detected by optical coherence tomography angiography in diabetic macular edema. *Invest Ophthalmol Vis Sci*. 2016;57(9):348–355.
38. Parravano M, De Geronimo D, Scarinci F, et al. Progression of diabetic microaneurysms according to the internal reflectivity on structural optical coherence tomography and visibility on optical coherence tomography angiography. *Am J Ophthalmol*. 2019;198(2):8–16.
39. Lammer J, Karst SG, Lin MM, et al. Association of microaneurysms on adaptive optics scanning laser ophthalmoscopy with surrounding neuroretinal pathology and visual function in diabetes. *Invest Ophthalmol Vis Sci*. 2018;59(13):5633–5640.
40. Hafner J, Salas M, Scholda C, et al. Dynamic changes of retinal microaneurysms in diabetes imaged with in vivo adaptive optics optical coherence tomography. *Invest Ophthalmol Vis Sci*. 2018;59(15):5932–5940.
41. Karst SG, Salas M, Hafner J, et al. Three-dimensional analysis of retinal microaneurysms with adaptive optics optical coherence tomography. *Retina*. 2019;39(3):465–472.
42. Stitt AW, Gardiner TA, Archer DB. Histological and ultrastructural investigation of retinal microa-

neurysm development in diabetic patients. *Br J Ophthalmol*. 1995;79(4):362–367.
43. Li H, Sampani K, Zheng X, et al. Predictive modelling of thrombus formation in diabetic retinal microaneurysms. *R Soc Open Sci*. 2020;7(8):201102.
44. Gao M, Hormel TT, Guo Y, et al. Perfused and non-perfused microaneurysms identified and characterized by structural and angiographic optical coherence tomography. *Ophthalmol Retina*. 2024;8(2):108–115.
45. Lee B, Choi W, Liu JJ, et al. Cardiac-gated en face Doppler measurement of retinal blood flow using swept-source optical coherence tomography at 100,000 axial scans per second. *Invest Ophthalmol Vis Sci*. 2015;56(4):2522–2530.
46. Bonfort T, Sturn P. Voxel carving for specular surfaces. *Proceedings Ninth IEEE International Conference on Computer Vision*. 2003;1:591–596.
47. Cai W, Lin M. Comparison of approaches based on optimization and algebraic iteration for binary tomography. *Computer Physics Communication*. 2010;181(12):1974–1981
48. Husvogt L, Yaghy A, Camacho A, et al. Ensembling U-Nets for microaneurysm segmentation in optical coherence tomography angiography in patients with diabetic retinopathy. *Sci Rep*. 2024;14(1):21520.
49. Zhang Q, Sampani K, Xu M, et al. AOSLO-net: a deep learning-based method for automatic segmentation of retinal microaneurysms from adaptive optics scanning laser ophthalmoscopy images. *Transl Vis Sci Technol*. 2022;11(8):7.
50. Nesbitt WS, Westein E, Tovar-Lopez FJ, et al. A shear gradient-dependent platelet aggregation mechanism drives thrombus formation. *Nat Med*. 2009;15(6):665–673.
51. Wang H, Chhablani J, Freeman WR, et al. Characterization of diabetic microaneurysms by simultaneous fluorescein angiography and spectral-domain optical coherence tomography. *Am J Ophthalmol*. 2012;153(5):861–867.
52. Savastano MC, Lumbroso B, Rispoli M. In vivo characterization of retinal vascularization morphology using optical coherence tomography angiography. *Retina*. 2015;35(11):2196–2203.
53. Bernabeu MO, Lu Y, Abu-Qamar O, Aiello LP, Sun JK. Estimation of diabetic retinal microaneurysm perfusion parameters based on computational fluid dynamics modeling of adaptive optics scanning laser ophthalmoscopy. *Front Physiol*. 2018;9:989.
54. Cai S, Li H, Zheng F, et al. Artificial intelligence velocimetry and microaneurysm-on-a-chip for three-dimensional analysis of blood flow in physiology and disease. *Proc Natl Acad Sci USA*. 2021;118(13):e2100697118.
55. Li H, Deng Y, Sampani K, et al. Computational investigation of blood cell transport in retinal microaneurysms. *PLoS Comput Biol*. 2022;18(1):e1009728.